



# Sweat-activated biocompatible batteries for epidermal electronic and microfluidic systems

A. J. Bandodkar<sup>1,2,16</sup>, S. P. Lee<sup>2,3,16</sup>, I. Huang<sup>1,16</sup>, W. Li<sup>3,16</sup>, S. Wang<sup>2</sup>, C.-J. Su<sup>2</sup>, W. J. Jeang<sup>1</sup>, T. Hang<sup>4</sup>, S. Mehta<sup>2</sup>, N. Nyberg<sup>5</sup>, P. Gutruf<sup>6,7,8,9</sup>, J. Choi<sup>10</sup>, J. Koo<sup>11</sup>, J. T. Reeder<sup>1,2</sup>, R. Tseng<sup>12</sup>, R. Ghaffari<sup>2,3,13</sup> ✉ and J. A. Rogers<sup>1,2,13,14,15</sup> ✉

**Recent advances in materials, mechanics and design have led to the development of ultrathin, lightweight electronic devices that can conformally interface with human skin. With few exceptions, these devices rely on electrical power to support sensing, wireless communication and signal conditioning. Unfortunately, most sources of such power consist of batteries constructed using hazardous materials, often with form factors that frustrate incorporation into skin-like, or epidermal, electronic devices. Here we report a biocompatible, sweat-activated battery technology that can be embedded within a soft, microfluidic platform. The battery can be used in a detachable electronic module that contains wireless communication and power management systems, and is capable of continuous on-skin recording of physiological signals. To illustrate the practical utility of our approach, we show using human trials that the sweat-activated batteries can operate hybrid microfluidic/microelectronic systems that simultaneously monitor heart rate, sweat chloride and sweat pH.**

Soft, skin-interfaced microsystems can provide precise, continuous measurements of physiological properties, with potential applications in healthcare, military readiness and sports<sup>1–3</sup>. Their advantage over conventional wearable systems stems from the ability to establish comfortable and intimate interfaces with the skin. With the exception of devices that rely on passive colorimetric sensors<sup>4–6</sup>, all skin-mounted platforms require a source of electrical power<sup>7–10</sup>. Coin cells and thin-film batteries remain the most widely used options, but their weight, thickness and size can hinder designs for skin-interfacing<sup>11–13</sup>. Flexible/stretchable energy-harvesting systems that generate power using body motion<sup>14,15</sup>, sweat<sup>16–18</sup> or ambient light<sup>19–22</sup> can overcome some of these problems. However, energy-harvesting approaches typically generate low and inconsistent energy output, rely on boost converters and require additional components for energy storage. Wireless harvesting of radiofrequency power from nearby antennas using far- or near-field coupling offers another potentially useful approach<sup>23–27</sup>, but the need to be close to a transmission antenna is a limitation.

The lack of a general solution for supplying power to skin-interfaced devices has driven research in advanced battery technologies in the form of textiles and flexible or stretchable sheets<sup>28</sup>, with a primary focus on lithium ion<sup>29,30</sup> or alkaline<sup>31–34</sup> chemistries. Similar platforms in supercapacitors rely on symmetric or asymmetric electrodes separated by polymeric membranes, typically loaded with alkaline electrolytes<sup>35,36</sup>. These technologies overcome some of the drawbacks associated with energy-harvesting approaches and demonstrate some utility in powering light-emitting diodes and simple

electronic circuits. Nevertheless, the scalability of these systems, their reliance on toxic chemicals and their potential for self-discharge during storage makes their practicality and safety uncertain.

A number of fluid-activated batteries have previously been developed<sup>37–40</sup> (Supplementary Table 1). However, none of these offer the ability to power advanced electronics for practical, body-worn digital diagnostic systems. In this Article, we report a thin, flexible and biocompatible sweat-activated cell (SAC) that produces sufficient power for state-of-the-art sensors, on-board data capture, processing, storage and wireless transmission of continuous-mode heart rate (HR) signals. Our SAC battery uses hybrid silicone and paper-based microfluidic systems to enable rapid sweat capture and storage. A flexible electronic module harvests the energy generated by the SACs. This module includes an active power management system that addresses challenges in power fluctuations associated with the dynamic processes of sweating and sweat initiation. To ensure high-fidelity digital recordings from the skin in the presence of sweat, electrical isolation circuits eliminate sources of interference that would otherwise arise from the unconventional working principles of the SAC. The system allows real-time HR measurements based on electrocardiogram (ECG) recordings, with performance that meets American National Standards Institute/Association for the Advancement of Medical Instrumentation (ANSI/AAMI) EC13:1992 standards.

## SAC components, design and properties

Figure 1a,b schematically illustrates the essential components of the SAC and its operating principles. The device includes a flexible

<sup>1</sup>Department of Materials Science and Engineering, Northwestern University, Evanston, IL, USA. <sup>2</sup>Center for Bio-Integrated Electronics, Querrey Simpson Institute for Bioelectronics, Northwestern University, Evanston, IL, USA. <sup>3</sup>Epicore Biosystems Inc., Cambridge, MA, USA. <sup>4</sup>State Key Laboratory of Metal Matrix Composites, School of Materials Science and Engineering, Shanghai Jiao Tong University, Shanghai, P. R. China. <sup>5</sup>Department of Mechanical Engineering, Northwestern University, Evanston, IL, USA. <sup>6</sup>Department of Biomedical Engineering, The University of Arizona, Tucson, AZ, USA. <sup>7</sup>Department of Electrical and Computer Engineering, The University of Arizona, Tucson, AZ, USA. <sup>8</sup>Bio5 Institute, The University of Arizona, Tucson, AZ, USA. <sup>9</sup>Neuroscience GIDP, The University of Arizona, Tucson, AZ, USA. <sup>10</sup>School of Mechanical Engineering, Kookmin University, Seoul, Republic of Korea. <sup>11</sup>School of Biomedical Engineering, Korea University, Seoul, Republic of Korea. <sup>12</sup>Department of Neurobiology, Northwestern University, Evanston, IL, USA. <sup>13</sup>Department of Biomedical Engineering, Northwestern University, Evanston, IL, USA. <sup>14</sup>Department of Electrical Engineering and Computer Science, Northwestern University, Evanston, IL, USA. <sup>15</sup>Feinberg School of Medicine, Northwestern University, Chicago, IL, USA. <sup>16</sup>These authors contributed equally: A. J. Bandodkar, S. P. Lee, I. Huang, W. Li. ✉e-mail: [rooz@epicorebiosystems.com](mailto:rooz@epicorebiosystems.com); [jrogers@northwestern.edu](mailto:jrogers@northwestern.edu)

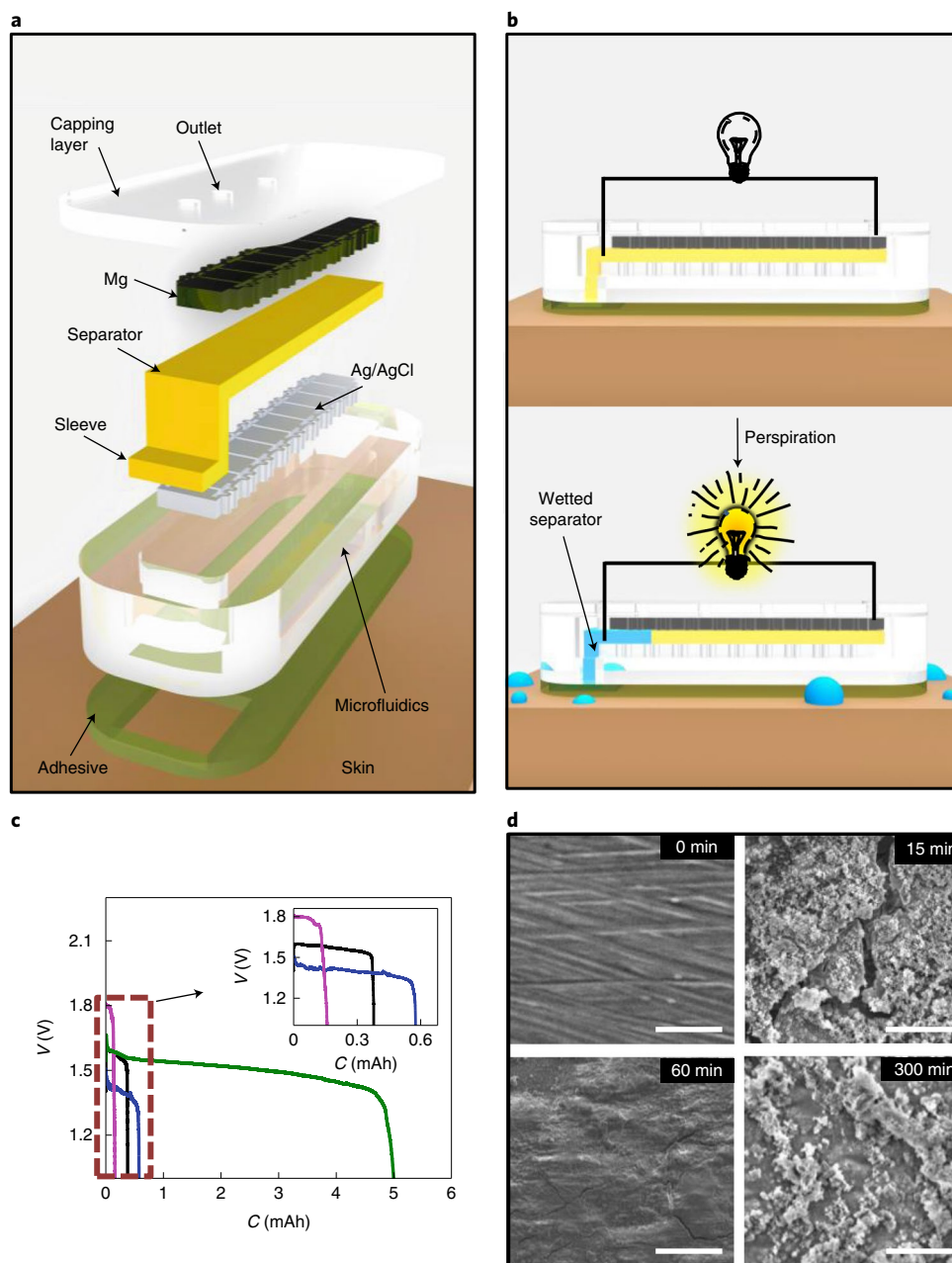


**Fig. 1 | Working principles and characteristics of an SAC.** **a**, Schematic exploded-view illustration of an SAC. **b**, Scheme showing the working principle of an SAC. **c**, Plots of discharge behaviours with different electrolytes, including phosphate buffer at pH 7 (black plot), 5-M sodium nitrate (blue plot), 5-M magnesium chloride (pink plot) and 0.35-M NaCl (green plot). *V*, voltage; *C*, capacity. Area, 1 cm<sup>2</sup>; discharge current, 1 mA. **d**, SEM images of the Mg anode after discharging at 1 mA for varying amounts of time. Scale bar, 50 μm.

Mg anode, a printed Ag/AgCl-based cathode and a thin, dry cellulose membrane impregnated with NaCl as a separator. In the absence of sweat, the dry separator maintains the SAC in an open electrical circuit condition. During perspiration, the membrane absorbs incoming sweat via a wicking sleeve in direct contact with the skin to provide the necessary aqueous electrolytic conditions for closing the circuit. In this state, the activated SAC produces usable electrical energy for powering electronic systems. The appeal of this platform stems from its skin-safe electrode and separator materials, and its use of sweat as both an activating cue and a natural, biocompatible electrolyte.

The high specific energy (~580 Wh kg<sup>-1</sup> with respect to the anode) and operational voltages (~1.6 V) supported by

these materials and designs enable miniaturized form factors (4 × 0.6 × 21 mm<sup>3</sup>) and minimal weight (~75 mg). In addition, the dry nature of the SAC in the absence of sweat overcomes issues associated with electrolyte leakage, self-discharge and poor shelf-life commonly encountered with conventional energy storage technologies. The SAC, with a materials cost of ~20 US cents, possesses a specific capacity (~67 Ah kg<sup>-1</sup>) comparable to that of a state-of-the-art commercial cell (CR2032; specific capacity ~73 Ah kg<sup>-1</sup>) due to its use of high-energy-density electrode materials, and the dry nature of the system in its inactivated mode, which excludes the weight of the electrolyte. The SACs can provide sufficient power for ~5 h operation, which is sufficient for most applications. The single-use nature of the microfluidic platforms

and associated biochemical assays also represents an excellent match to SAC-based primary batteries.

The electrolyte is generally the most toxic component in energy storage devices. Thus, in developing a biocompatible, skin-interfaced energy source that activates when needed—that is, upon release of sweat in sports/fitness applications—a user's own perspiration provides an ideal alternative. Naturally excreted salts render sweat conductive, with frequency-dependent conductivities usually between 1 and 10 mS cm<sup>-2</sup> (ref. 41). Successful development of a sweat-based energy source relies critically on complementary cathodic and anodic materials that efficiently perform with such bioderived, near-neutral-pH electrolytes. Our SACs rely on period-three metal anodes coupled with suitable cathode materials to generate appreciable electrical power with sweat as the electrolyte. Preliminary tests that compare capacities with different combinations of anodes (Mg, aluminium) and cathodes (carbon, platinized carbon, Ag/AgCl, copper, Prussian blue), using 100-mM NaCl solutions as a proxy for sweat, reveal that the Mg–Ag/AgCl system offers excellent performance (Supplementary Fig. 1a). Supplementary equations (1) and (2) provide half-cell reactions for the Mg–Ag/AgCl cell.

Sweat composition varies with physiological state, diet, time of day, season, environmental conditions and other factors<sup>42–44</sup>, each of which may lead to instabilities in power generation in SACs. As a means to overcome this issue, the thin cellulose-based separators introduced here include preloaded quantities of salts. Figure 1c and Supplementary Fig. 1b show data aimed at identifying the ideal skin-friendly salt for this purpose. The concentrations selected for the different electrolytes follow from results reported previously for Mg cells<sup>45</sup>. The cell with the 5-M MgCl<sub>2</sub> electrolyte produces the highest initial operating voltage (1.8 V) and may be attributed to a reduction in the kinetics of the Mg oxidation associated with the high concentration of magnesium ions, per Le Chatelier's principle. The low voltage for the cell with 5-M NaNO<sub>3</sub> probably stems from the absence of chloride ions in the electrolyte and associated increased degradation of the cathode. These data clearly indicate that the NaCl-based electrolyte supports the longest stable discharge periods. Here, the chloride provides a stabilizing effect on the Ag/AgCl cathode, again on the basis of Le Chatelier's principle. Although previous reports show deteriorative effects of chloride electrolytes on Mg<sup>46</sup>, results illustrated in Fig. 1c and Supplementary Fig. 1b indicate that the benefits from cathode stabilization exceed these negative effects on the anode, as long as chloride concentrations in the electrolyte remain below a threshold value (discussed later).

Supplementary Fig. 1c displays the discharge profiles for cells with increasing concentrations of NaCl. The data show that the performance saturates at around 350 mM. Fundamental characterization of the Mg–Ag/AgCl cell therefore utilizes 350-mM NaCl as the electrolyte (Supplementary Figs. 1d,e and 2). Even though this concentration is higher than physiological levels in sweat, the SAC construction involves preloading of the separator with sufficient quantities of NaCl to ensure that performance is independent of the sweat electrolyte concentration and conductivity (discussed later). Supplementary Fig. 1d displays the capacities for cells with fixed Mg anode thickness (100 μm) and different thicknesses of Ag/AgCl layers. On the basis of the results, cells used in the following demonstrations utilize Mg (100 μm) and Ag/AgCl (300 μm), as these thicknesses provide optimal performance without substantially increasing the total device dimensions. Additional studies illustrate that native Mg hydroxide layer (MgHL) has negligible impact on SAC performance and suggest a long shelf-life, without pretreatment of the anode (Supplementary Fig. 1e). Supplementary Fig. 2a illustrates the SAC operational lifespan for various discharge currents. The data reveal a C-rate of ~4.5 C for the SAC.

Electrochemical impedance spectroscopy (EIS) and scanning electron microscopy (SEM) are valuable tools for characterizing battery behaviours<sup>47,48</sup>. Supplementary Fig. 2b displays Nyquist

plots for a pristine SAC and for an SAC after 5 min of 1-mA discharge. The data show a high-frequency semicircle (*S*<sub>1</sub>) obscured by a medium-frequency semicircle (*S*<sub>2</sub>) for the pristine SAC, which becomes more prominent after 5 min of discharge. Charge transfer (CT) processes across the metal–hydroxide and hydroxide–electrolyte interfaces probably account for *S*<sub>1</sub> and *S*<sub>2</sub>, respectively<sup>49,50</sup>. These observations suggest that initial CT across the metal–hydroxide interface for a pristine SAC is poor due to the presence of naturally formed MgHL. Discharging the SAC generates cracks in this MgHL and allows penetration of the electrolyte to form direct contacts with the underlying Mg. This behaviour results in CT across the metal–hydroxide interface, represented by the appearance of *S*<sub>1</sub>. The total impedance at 1 kHz (*Z*<sub>1kHz</sub>) and the phase shift (*θ*) during the lifespan of the SAC appear in Supplementary Fig. 2c. The rapid decrease of *Z*<sub>1kHz</sub> to a stable value indicates that cracks swiftly form in the MgHL, thereby allowing facile CT.

An initial decrease in *θ* followed by an increase to values almost similar to those for a pristine SAC during the first 2 h of discharge suggests an initial decrease in the capacitive nature of the electrode–electrolyte interface followed by an increase. The initial dip in *θ* may be due to rapid cracking of the pristine MgHL at the beginning of the discharge. The subsequent increase in *θ* can be attributed to formation of new MgHL, thus increasing the area of the MgHL and the capacitive nature of the electrode–electrolyte interface. As the newly formed MgHL densifies, it impedes CT kinetics. To maintain a constant discharge current, cracks eventually develop across the surface to expose Mg, which is consistent with a decrease in *θ* after 2 h.

SEM results presented in Fig. 1d, along with energy dispersive X-ray spectroscopy studies summarized in Supplementary Fig. 2d, further support the conclusions drawn from EIS. Specifically, the SEM data reveal a cyclical trend of smooth and cracked Mg surfaces at different times of discharge, as predicted by EIS. Additional SEM images captured from different regions of the anode after 15 and 60 min of discharge illustrate the homogeneous presence of cracks and resmoothed morphology over the anode depending on the duration of discharge (Supplementary Fig. 2e,f). These observations are consistent with those of previous research on corrosion of metal electrodes<sup>49,50</sup>.

Additional studies examine the SAC set-up in a form factor compatible with use in skin-interfaced devices. The electrodes comprise a series of 2 × 2.4-mm<sup>2</sup> pads interconnected via serpentine structures, with overall dimensions of 4 × 21 mm<sup>2</sup> (Supplementary Fig. 2g). The serpentine connects adjacent pads via the side edges, to impart excellent flexibility with high areal coverage (~66%), essential for high energy density. The structured SAC electrodes and the separator between them (dimensions 25 × 6 mm<sup>2</sup>; maximum liquid holding volume 45 μl) stack vertically within an elastomeric microfluidic system (Fig. 1a). The microfluidics includes a single inlet for electrolyte (that is sweat) to enter the chamber and activate the SAC via capillary wicking of the separator.

Multiple outlets defined on the capping layer permit the release of excess electrolyte and hydrogen gas by-products (Fig. 1a,b). The wicking mechanism is crucial during the initial phase of sweating to ensure rapid delivery of the sweat into the microfluidic system and to minimize delay in the SAC activation. The system does not require replacement of the separator once it is saturated because the outlets provide routes to expel excess sweat and allow fresh sweat to enter the chamber. Preliminary on-body studies using devices with only a single outlet indicate poor performance compared with similar devices with multiple outlets (Supplementary Fig. 3), probably due to restricted release of hydrogen by-product. Devices with single outlets also exhibit expansion of the elastomeric membranes during discharge, visible by eye, suggesting the build-up of gas within the chamber. Controlled investigations use NaCl solution injected at fixed flow rates into the SAC while discharging at 1 mA. The concentrations of these solutions (0–120 mM) and the

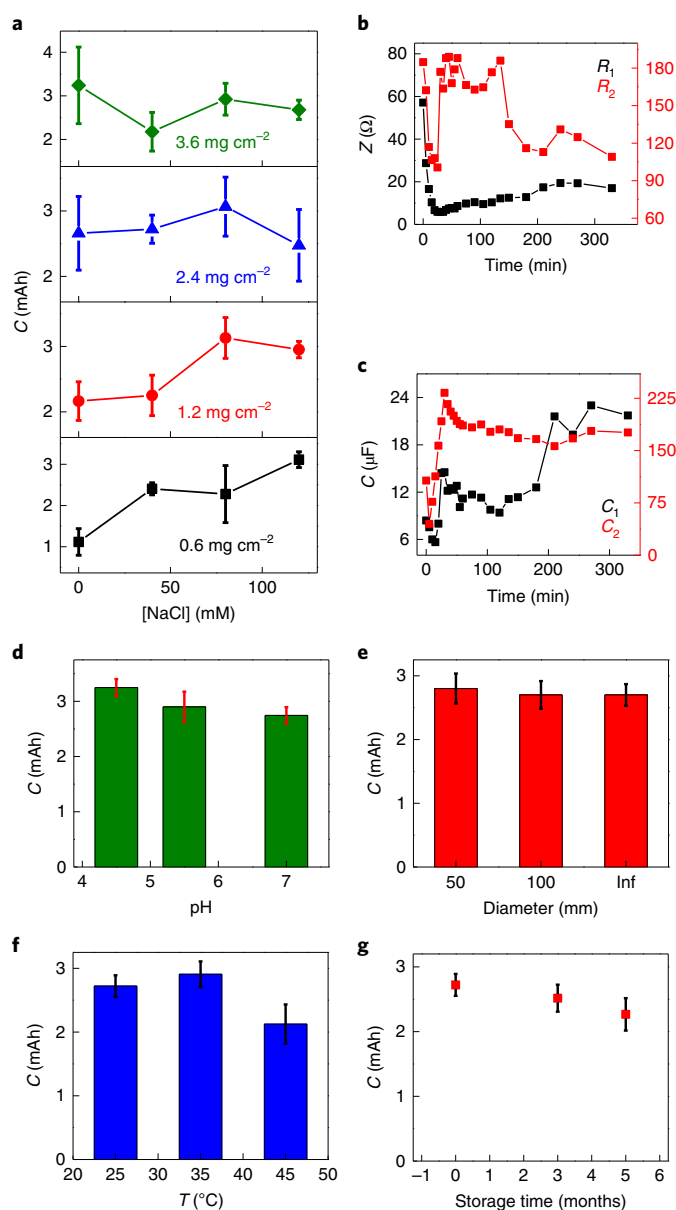


**Fig. 2 | Discharge properties and EIS studies of SAC.** **a**, Effect of NaCl loading within the separator on the lifespan of the SAC. **b,c**, Evolution of resistances (**b**) and capacitances (**c**) of the SAC with time. **d–g**, Effect of pH of the incoming solution (**d**), bending (**e**), temperature (**f**) and storage (**g**) on SAC capacity. System: single electrochemical cell with patterned Mg and AgCl electrodes and separator (Fig. 1a,b and Supplementary Fig. 2g); area  $0.46 \text{ cm}^2$ ; flow rate  $1 \mu\text{l min}^{-1}$ ; discharge current =  $1 \text{ mA}$ .

flow rates ( $1 \mu\text{l min}^{-1}$ ) are comparable to those measured in natural sweating processes<sup>51,52</sup>.

Figure 2a demonstrates the effect of incoming electrolyte concentration on the capacity of SACs with separators that contain various quantities of preloaded salt. The data reveal that the capacity is independent of the concentration for SACs with a preloaded NaCl concentration of  $2.4 \text{ mg cm}^{-2}$ . We notice a decrement in the SAC capacity at NaCl concentrations above  $100 \text{ mM}$  for SACs with  $2.4 \text{ mg cm}^{-2}$  and  $3.6 \text{ mg cm}^{-2}$  salt loading. This behaviour can be attributed to the high total effective chloride concentration in the SACs and an associated corrosive effect of the chloride ions on the anode that overcomes their stabilizing effect on the cathode. The reduced capacity of the SACs at such chloride concentrations should

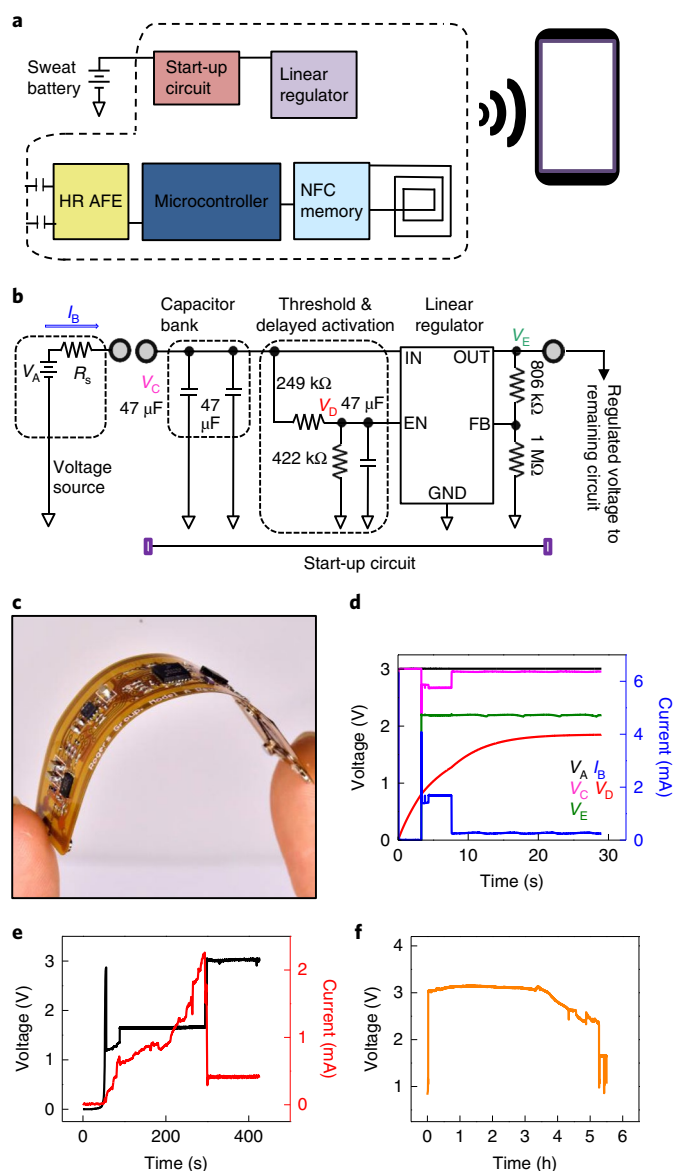
not, however, be a major issue for practical applications, since the average range of chloride concentrations for sweat is typically well below this threshold limit<sup>51</sup>. The capacity of an optimized SAC (area  $0.46 \text{ cm}^2$ ) with a form factor compatible with use in skin-interfaced devices, as shown in Fig. 1a,b, is  $\sim 3 \text{ mAh}$ . This value is lower than that recorded in preliminary studies using set-ups with comparatively large electrodes (area  $1 \text{ cm}^2$ ).

Figure 2b,c illustrates the resistance and capacitance dynamics for an SAC during exposure to incoming solution ( $40\text{-mM NaCl}$  at  $1 \mu\text{l min}^{-1}$ ). In the first  $\sim 30 \text{ min}$ , all of the relevant parameters ( $R_1$ ,  $R_2$ , CT resistance;  $C_1$ ,  $C_2$ , capacitance corresponding to the high-frequency and low-frequency semicircles, respectively) monotonically decrease. As the electrolyte travels across the separator, the electroactive area between the electrodes increases and the conductivity between them improves, leading to a decrease in CT resistance. The continuous decreases in  $C_1$  and  $C_2$  during this time suggest that, although the electroactive area increases, the initial formation of surface cracks in the MgHL leads to substantial disruption in the capacitive nature of the interface. After  $\sim 30 \text{ min}$  the separator becomes fully hydrated, causing the formation and fracture of the MgHL to dominate the properties. Here,  $R_2$ ,  $C_1$  and  $C_2$  increase while  $R_1$  remains nearly constant, with a slight increase at the end of the study. These observations suggest that the CT kinetics remain mostly unaffected across the electrode–electrolyte interface. The increase in  $C_1$ ,  $C_2$  and  $R_2$  point to the formation of new MgHL. Toward the end of the lifespan of the SAC, decreases in  $R_2$  can be attributed to cracking of the formed MgHL. A slight increase in  $R_1$  and  $C_1$  may result from oxidation-led weakening of the Mg electrical contact (terminal pad of the electrode). The SAC ultimately fails when the electrical connection to the anode is lost as the contact becomes completely oxidized.

The effects of pH, temperature, mechanical bending and storage appear in Fig. 2d–g. All of these experiments utilize artificial sweat (Pickering Laboratories). These studies reveal that the performance is largely independent of electrolyte composition. The data indicate, however, a slight loss of capacity of the SAC at high ambient temperatures ( $\geq 45^\circ \text{C}$ ), perhaps due to increased rates of evaporation under low-flow-rate conditions ( $1 \mu\text{l min}^{-1}$ ), resulting in increased internal resistance ( $R_s$ ). The performance of the SACs suffers similar negative effects in high-pH solutions. Here, the MgHL exhibits increased stability, thereby impeding formation of cracks during discharge. As suggested by the EIS results, resiliency to MgHL cracking may inhibit the penetration of the electrolyte and subsequent electrical contact with the underlying Mg, leading to an increase in  $R_s$  and a concomitant decrease in performance.

### Flexible wireless electronics for continuous HR sensing

A reusable, flexible electronic module for capturing and storing HR information using the SAC and transmitting the data via near-field communication (NFC) protocols serves as a demonstration system. The thin, lightweight module (circuit diagram in Fig. 3a) facilitates mounting onto skin-interfaced microfluidic systems that support an SAC-based battery (two SACs in series) for energy generation, and ECG electrodes for signal acquisition. Upon wetting with sweat, the battery enters a closed-circuit mode and activates the electronic system. The start-up circuit (Fig. 3b) delays activation for a maximum time constant of  $7.3 \text{ s}$ , and also ensures that a minimum voltage threshold of  $1.27 \text{ V}$  is met to allow the  $94\text{-}\mu\text{F}$  capacitor bank ( $V_C$ ) to fully charge. A photograph of the module appears in Fig. 3c. Unlike conventional batteries, the  $R_s$  of the SAC changes continuously, especially during the initial period of activation, as indicated by the EIS studies. Such variations in  $R_s$  can lead to unpredictable behaviour in standard start-up circuits. Figure 3d and Supplementary Fig. 4 display evidence of the adaptability of the custom circuit introduced here, wherein the system exhibits start-up capabilities with different values of  $R_s$ .



**Fig. 3 | Power management circuit and its characteristics.** **a**, Simplified block diagram of the electronic module. **b**, Magnified schematic of the start-up circuit. GND, circuit ‘common’ or ground; EN, enable pin of the regulator; FB, feedback node that sets the regulated voltage  $V_E$ . **c**, Photograph of the flexible electronic module. **d**, Node voltages during start-up for a battery with an internal resistance of  $200\ \Omega$ .  $V_A$ , ideal battery voltage;  $V_C$ , voltage of a typical sweat-activated battery with  $R_s = 200\ \Omega$ ;  $V_D$ , enable pin voltage of the regulator;  $V_E$ , regulated system voltage;  $I_B$ , battery current. **e**, Real-time voltage and current draw from the SAC-based battery during start-up. **f**, Battery voltage versus time plot acquired during continuous powering of the electronics with the SAC-based battery. Flow rate  $1\ \mu\text{l}\ \text{min}^{-1}$ .

When a voltage ( $V_A$ ) is applied at time  $t=0$ , the resistor divider ( $249\ \text{k}\Omega$ ,  $422\ \text{k}\Omega$ ) reduces the battery voltage ( $V_C$ ) to a value  $V_D = 0.62 V_C$  at the enable pin of the linear regulator. Together, the  $47\text{-}\mu\text{F}$  capacitor and the divider create the time delay observed by the transient response of  $V_D$ , whose value must reach  $0.8\ \text{V}$  before delivering voltage to the rest of the system.  $V_D$  follows the characteristic response of a capacitor charging ( $V_D = 0.62 V_C (1 - e^{-t/379})$ ;  $t$  is in seconds). The effect is twofold. First, the capacitor layout within the start-up circuitry shifts the burden of supplying instantaneous

current ( $I_B$ ), which the electronics require, from the SAC-based battery to the precharged capacitor bank. Second, the minimum threshold voltage dictated by the linear regulator prevents premature activation until there is sufficient sweat in the microfluidic chamber to support the necessary current draw.

This approach enables the execution of initial tasks, such as clearing the electrically erasable programmable read-only memory (EEPROM), which requires  $2\ \text{mA}$  for  $5\ \text{s}$ . Subsequently, the system switches to low-power mode ( $300\ \mu\text{A}$ ). With increasing  $R_s$ , the electronics require a higher battery voltage. However, benchtop tests indicate that the system can operate even with  $R_s$  as large as  $500\ \Omega$  (Supplementary Fig. 4). The EIS studies reveal that  $R_s$  falls below this value within a couple of minutes of activation, thus enabling the rapid powering of the electronics even with small quantities of sweat. Figure 3e presents experimental data to support this statement. The study involves injecting  $40\text{-mM}$  NaCl solution in  $1\text{-}\mu\text{l}$  aliquots into a dry SAC-based battery while connected to the electronics. After injection of  $2\ \mu\text{l}$  of NaCl solution, the battery voltage reaches  $\sim 1.5\ \text{V}$  and maintains this value until it rises to  $3\ \text{V}$  upon addition of a total of  $5\ \mu\text{l}$ . At this point, the electronics activate, shift to the low-power mode, and operate continuously.

In addition to the start-up circuit, the microcontroller firmware helps avoid high current draw from the battery by activating the HR analogue front end (AFE) and the NFC tag sequentially, with a time step in between. Thereafter, the firmware switches the microcontroller to its very low-power run mode, which operates at a reduced system bus frequency. Here, the long-term power draw is determined by the software state machine that instructs the microcontroller to deactivate unneeded circuits in the absence of a task, to reduce current draw (Supplementary Fig. 5a). A periodic timer awakens the CPU, driving the state machine to manage sampling of the ECG, detection of the heartbeat, storage of the HR data and system housekeeping. Figure 3f demonstrates the efficacy of the state-machine algorithm in maximizing the operational lifespan of the SAC. For designs reported here, the SAC-based battery can power the electronics for  $\sim 5\ \text{h}$ , which is sufficient for most applications in athletics and general fitness.

The sweat can provide a conductive path between the SACs and the ECG electrodes (Supplementary Fig. 5b), with the possibility to inadvertently create a large differential or common-mode d.c. voltage relative to the millivolt-level ECG signal. This effect leads to erratic results if the d.c. voltage across the ECG electrodes and the SACs exceeds the operating voltage limit of the HR AFE. A solution to this problem involves a.c.-coupling the HR AFE input to each of the ECG electrodes (Supplementary Fig. 5c). The result is electrical isolation of the HR AFE from the d.c. voltage generated across the ECG electrodes and the SACs. To further reduce crosstalk, the node between each input capacitor and each HR AFE’s input pin is driven using a pseudo-right-leg drive scheme that improves common-mode rejection and maintains the input voltage of the AFE within the supply rails. The characteristics of the electronic module for measuring HR appear in the Supplementary Information and Supplementary Fig. 6a–c.

### SAC-powered hybrid microfluidic/microelectronic system

A demonstration of the practical application of the SAC technology utilizes a hybrid microfluidic/microelectronic system that integrates biochemical and biophysical sensors for simultaneous, comprehensive tracking of physiological biomarkers pertinent to general fitness and sports (Fig. 4a,b). The device consists of two main components. The first is a soft, disposable microfluidic patch that supports an SAC-based battery, an array of microchambers for colorimetric sensing of pH and chloride concentrations, and ECG electrodes for HR monitoring. The second is the previously described reusable electronic module that electromechanically connects to the

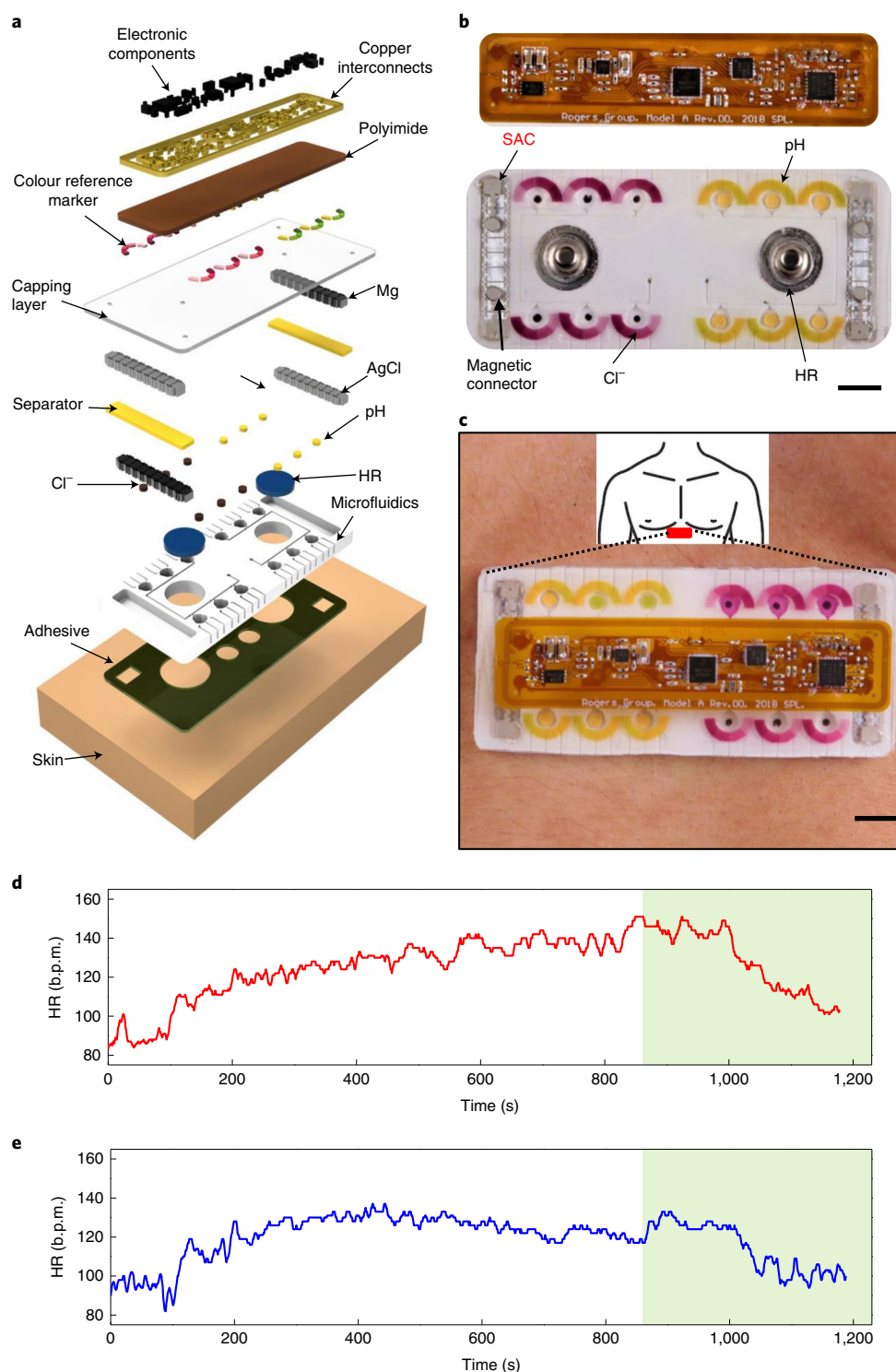


**Fig. 4 | SAC-powered, skin-interfaced hybrid microfluidic-microelectronic system.** **a**, Schematic exploded-view illustration of an SAC-powered hybrid microfluidic-microelectronic, skin-interfaced device for simultaneous monitoring of HR, sweat chloride ( $\text{Cl}^-$ ) and sweat pH. **b**, Image of a complete system. Scale bar, 1 cm. **c**, Photograph of the device mounted on the chest. Scale bar, 1 cm. **d,e**, Real-time HR captured by a device on human subjects during cycling. b.p.m., beats per minute. Green region: postcycling cool-down.

SACs via thin magnets (diameter = 2 mm; height = 1 mm) and to the ECG electrodes through snap button connectors for capture and storage of HR.

The chamber housing the SAC comprises of a thin rectangular inlet (1 mm wide and 2.5 mm long) at the corner where the cathode connects the electronics. Strategic positioning of the inlet for

the SAC chamber near the cathodic connection position delays the onset of Mg corrosion at the anodic connection that eventually causes its electrical disconnection. The anode faces upwards and lies close to the outlets to support rapid effusion of the hydrogen gas. The separator includes a sleeve that passes through the inlet and contacts the skin to ensure efficient wicking of sweat into the

chamber. The HR sensor includes two commercial ECG electrodes flanking the centre of the patch.

Within the microfluidic network, a series of microchambers house individual colorimetric chloride and pH assays. Capillary burst valves separate the microchambers for time-sequential colorimetric biochemical assessment of sweat composition. Supplementary Fig. 6d, e illustrates the linear dependence of the lightness ( $L$ ) and  $R$  values acquired from RGB colour analysis code applied to digital images of the assay colour as a function of chloride concentration and pH value, respectively. Scanning a smartphone with ST25 NFC Tap application software (STMICROELECTRONICS) allows wireless acquisition of the stored HR profile while the phone's camera captures assay colours for robust estimation of chloride and pH levels by image analysis. As illustrated in Figs. 1a,b and 4b, the sweat from the SACs is released from multiple outlets present in the capping layer above the SAC chamber. Each of the colorimetric assay chambers has its own set of three outlets on the side of the patch (Supplementary Fig. 7). The physical separation between outlets for the colorimetric assays and the SACs minimizes the potential intermixing of the sweat from these chambers.

Human trials involve healthy subjects (four males) cycling on a stationary bike while wearing the device on the chest (shaven and cleaned via alcohol wipes) with the ECG electrodes positioned at the  $V_1$  (right of the sternum) and  $V_2$  (left of the sternum) (Fig. 4c). These studies follow guidelines set by the Institutional Review Board at Northwestern University (STU00208494). The trials reveal that the sweat activates the SACs and powers the electronics within the initial minutes of sweating and well before the filling of the microchambers with colorimetric assays. On the basis of our studies, 10–15 min of mild physical activity can yield power sufficient for operation of the electronics. Although the present system design targets active users, the concept of SACs to power electronics can also apply to sedentary users via advanced sweat capturing methods<sup>53</sup>. This filling behaviour highlights the efficacy of the separator sleeve, which directly contacts the skin, in rapidly wicking small quantities of sweat into the SAC chamber.

Figure 4d,e illustrates representative HR data acquired during these trials. Following SAC activation, the data indicate elevated HR values for all subjects, within typical ranges for healthy adults during exercise<sup>54</sup>. During a brief postcycling cool-down period, the data reveal gradual declines in HR as expected. Supplementary Fig. 8 exhibits closeup images of colorimetric assays and the estimated concentrations obtained during the human trials. These values are within the physiological expectation reported previously<sup>4,55</sup>. Supplementary Fig. 9 illustrates additional human trials that compare HR signals captured from the hybrid device with that acquired from a commercial wearable system (Polar H7). The results highlight the potential of SAC-powered hybrid microfluidic/microelectronic systems for simultaneously capturing both biochemical and biophysical information for comprehensive physiological monitoring. Importantly, these studies illustrate the use of SACs as practical, biocompatible power sources for skin-integrated electronics.

## Conclusions

We have developed a lightweight, biocompatible, sweat-activated power source as an alternative to conventional energy storage devices, for use in epidermal electronic and microfluidic systems. Careful selection of the materials, device architectures, cell assembly layouts and microfluidic housings enables rapid activation of the SACs with performance largely independent of sweat composition. In the absence of sweat, the SACs are naturally dry, mitigating concerns regarding self-discharge, electrolyte leakage and storage shelf-life. The module can be worn on human skin and includes circuitry that allows interference-free acquisition of physiological signals, as well as their analysis and wireless transmission.

## Methods

**Fabrication of SAC.** The fabrication began with use of an ultraviolet laser (LPKF U4) to define the anodes using a 100- $\mu\text{m}$ -thick sheet of magnesium (Alibaba), and substrates for the cathodic current collectors from a 75- $\mu\text{m}$ -thick sheet of polyimide (Argon). Subsequent application of Ag/AgCl ink (E2414, Ercon) to the patterned polyimide structures resulted in conductive cathodic current collectors. Separately, screen printing a Ag/AgCl ink onto laser printer tattoo paper (HPS LLC) using a 300- $\mu\text{m}$  rectangular stencil, sequential baking at 65 °C and 80 °C each for 1 h, cutting into rectangular pads (2×2.4 mm<sup>2</sup>) using a CO<sub>2</sub> laser (Universal Laser Systems), releasing the pads from the tattoo paper with the addition of water, bonding the pads to the Ag/AgCl-coated polyimide current collector through the application of conductive Ag/AgCl ink and baking at 80 °C for 10 min formed the cathode. Applying varying volumes of 350-mM NaCl solution to laser-patterned cellulose paper (Kimtech Science Kimwipes, Kimberly-Clark Professional), followed by thorough drying in ambient conditions, yielded separators with different NaCl salt loadings. Placement of the separator between the anode and cathode prevented short-circuiting, while slight extension of the separator through the inlet of the microfluidic patch created a sleeve for wicking sweat directly from the skin.

**Fabrication of the soft microfluidic system.** The process began with cleaning a 4" silicon wafer sequentially using isopropyl alcohol, acetone, deionized water and isopropyl alcohol again. Spin coating and baking at 110 °C for 5 min on a hot plate formed a film of photoresist (KMPR 1010; Microchem) with thickness of ~15  $\mu\text{m}$ . Exposing the wafer to ultraviolet light through a photomask, baking at 110 °C for 3 min in a closed chamber, baking again at 110 °C for 2 min in an open system and then immersing in a developer solution (AZ 917 MIF; Integrated Micro Materials) patterned the photoresist into the desired geometries. Deep reactive ion etching (STS Pegasus ICP-DRIE, SPTS Technologies) generated ~750- $\mu\text{m}$ -deep microtrenches in the silicon. Spin coating a layer of poly(methylmethacrylate) (PMMA; Microchem) at 2,000 r.p.m. for 30 s and baking at 180 °C for 3 min defined a release layer on this structure, for use as a mould. Mixing 5-wt% white pigmented silicone (Reynolds Advanced Materials) with a transparent precursor of polydimethylsiloxane (PDMS; 10:1; SYLGARD 184, Dow Corning) yielded a white silicone suspension. Uniform manual casting of 7 g of this PDMS mixture onto the mould and curing at 70 °C for 1 h created, upon release, a ~750- $\mu\text{m}$ -deep, flexible structure with relief geometries that form the microchambers in the microfluidic platform. Mechanical punches created two 1-mm-diameter holes through the PDMS membrane to define inlets for colorimetric assays and two 10-mm-diameter holes to accommodate ECG electrodes. Separate 1×2.5-mm<sup>2</sup> rectangular holes acted as inlets for the SAC chambers. Pouring a transparent PDMS precursor (10:1) on a silicon wafer coated with PMMA, spin coating at 200 r.p.m. for 30 s and curing at 70 °C for 1 h yielded a uniform ~300- $\mu\text{m}$ -thick film as a capping layer for the microfluidic design. A second layer of PDMS (60:1) spin cast on top of the cured membrane at 1,000 r.p.m. and cured at 70 °C for 1 h created an adhesive coating for bonding to the moulded microfluidic base. A mechanical punch (diameter 1.5 mm) defined five equally spaced outlets on the PDMS cap to allow release of excess sweat and hydrogen gas from the SAC chambers. A separate mechanical punch (diameter 2 mm) formed electrical vias at the extreme ends to interface the SAC with the electronic module via magnetic connectors. The magnetic connectors resulted from laser patterning a sheet of polyimide (thickness 75  $\mu\text{m}$ ) into serpentine interconnects, bonding magnets (diameter 2 mm; thickness 1 mm) to the interconnects and finally applying a thin layer of silver paint to the completed structure. Another mechanical punch (diameter 6 mm) formed holes flanking the centre of the cap to accommodate the snap connectors of the ECG electrodes.

Sequentially stacking the Ag/AgCl cathode, salt-loaded separator and Mg anode within designated chambers formed the embedded SACs. Placing colorimetric assays in their respective microchambers completed the fabrication of the colorimetric assays. Laminating the adhesive side of the capping layer directly to the microfluidic structure sealed the components within the device. Filling the electrical vias with silver epoxy, interfacing the magnetic connectors and finally curing the epoxy at ambient conditions for at least 4 h resulted in permanent bonds between the magnetic connectors and the SACs for facile reversible electrical connection with the electronics module. A pair of excised commercial gel ECG electrodes (3M Red Dot) with snap connectors served as HR sensors. A CO<sub>2</sub> laser (Universal Laser Systems) defined holes in a skin adhesive film (medical tape 1524, 3M) for the sweat inlets for both assays, the SACs and for the HR sensor. A plasma treatment of the skin-adhesive membrane and the microfluidic platform using a corona generator produced hydrophilic surfaces to facilitate bonding of the two layers. A commercial laser printer (Konica Minolta C454 PS colour) produced colour reference markers on a 25- $\mu\text{m}$ -thick polyester film (FLX000464; FLEXcon). Finally, laminating the colour reference markers on top of the capping layer such that the markers encircle the colorimetric assays completed the microfluidic assembly process.

**Fabrication of the wireless electronic module.** Fabrication of the flexible, planar electronics module began with a polyimide film (thickness 25  $\mu\text{m}$ ) bonded to copper foil (thickness 18  $\mu\text{m}$ ) on each side (DuPont Pyralux KP182518E). Application of printed circuit board processing techniques produced patterns

of copper (thickness 10  $\mu\text{m}$ ) plated with gold (thickness 50 nm). A thick coverlay (Grace Electron, CNV018XMK1, thickness 30.5  $\mu\text{m}$ ) applied to both sides, and gang cutouts formed on the top side, exposed the integrated circuit components. Application of solder paste (Kester, EP256) through a laser-cut stainless-steel stencil (thickness 3 mm) enabled precise placement of components (NXP MKL02Z32VFK4 microcontroller, AD8232 HR AFE integrated circuit, TPS78001DRV linear regulator and STMicroelectronics M24LR64E-R NFC EEPROM) and subsequent reflow soldering of the entire flex printed circuit board. Finally, attaching magnets and snap connectors to the designated contact pads of the electronic module using silver epoxy allowed reversible connection to the SACs and the HR electrodes in the soft microfluidic patch, respectively.

**Firmware for battery-free NFC-based electronics.** The embedded software for the electronics module capitalized on a state-machine design pattern. The firmware, written in C, leveraged NXP Kinetis libraries and the Keil  $\mu\text{Vision}$  integrated development environment. Firmware microcode runs in low-power mode and operates at the lowest CPU clock frequency during initialization. Unused microcontroller ports are set to high  $z$ , unused peripherals are deactivated and active peripherals are set to low power to maximize power efficiency. Upon start-up, the firmware turns on the AFE front end and the NFC tag sequentially, with a time step in between to avoid high in-rush current. Thereafter, the firmware rapidly switches the microcontroller to its very low-power run mode to achieve a reduced system bus frequency. The absence of a required task causes the system to switch into sleep mode. A periodic timer awakens the CPU, driving the state machine to manage ECG data sampling, heartbeat detection, HR data storage and system housekeeping (Supplementary Fig. 5a).

**ECG capture program.** A program written in LabVIEW 12 communicated with a National Instruments USB-6216 data acquisition system to capture the narrow-band ECG conditioned by the AD8232 (AFE). Analysis of the captured data enabled characterization of the changes in ECG morphology as subjects exercised and moved rapidly. Exporting the ECG data saved in the National Instruments Technical Data Management Streaming format into comma-separated values (CSV) files facilitated data plotting and analysis. For improved accuracy in calculating HR, requesting the subjects to be at rest for the first 2 min of activation of the electronics by the SACs enabled the algorithm to identify noise levels for rejection of erratic signals from motion artifacts (similar to the initial learning period required by commercially available, patient monitoring ECG systems such as a GE Dash 3000).

**HR algorithm tuning program.** Development of the desktop application for refining the HR detection algorithm for use during exercise utilized the C programming language using the Microsoft Visual Studio integrated development environment. The program read in the ECG data files in CSV format, allowing side-by-side comparison of HR values following modifications made to the HR algorithm.

**HR measurement accuracy studies.** A Data Science Automation ECG simulator program in conjunction with a National Instruments PXI-6289 data acquisition system resulted in an ANSI/AAMI EC13:1992-compliant ECG waveform that was divided down by a 100- $\Omega$ /10-k $\Omega$  resistor divider and fed into the AFE of the electronics. Comparison of the detected HR with the known ECG QRS rate (from the ECG simulator) allowed verification of the accuracy of the HR detection algorithm.

**Development of the colorimetric assays.** The chloride assay consisted of 50 mg of silver chloranilate (MP Biomedicals) dispersed in 200  $\mu\text{l}$  of a 2-wt% polyhydroxyethylmethacrylate (Sigma-Aldrich) suspension in methanol. Drop-casting 1  $\mu\text{l}$  of this assay into chambers in the microfluidic platform prepared the system for sensing. The pH assay comprised 4 ml of universal pH dye (Fisher Scientific), 274 mg of polyvinyl chloride (average molecular mass  $\sim$  233,000; Sigma-Aldrich), 635  $\mu\text{l}$  of *o*-nitrophenyloctylether (Sigma-Aldrich) and 508  $\mu\text{l}$  of Aliquat (Sigma-Aldrich) in 10 ml of tetrahydrofuran (Sigma-Aldrich). Dip-coating a filter paper (Sigma-Aldrich) into this solution for 10 s and air drying for 15 min followed by cutting the paper into circular pads with a mechanical punch (diameter 2 mm) and finally placing each pad in respective microchambers concluded the pH assay fabrication.

**Data collection and analysis.** An electrochemical analyser (PGSTAT128N, Metrohm) enabled electrochemical characterization of the SACs. A data acquisition system (National Instruments) with custom LabView software captured narrow-band ECG morphology for optimization of the HR algorithm and characterization of the electronic module. Human trials involved using a Samsung S7 smartphone to wirelessly collect the HR data stored in the memory of the electronic module while the phone's camera allowed capture of the colorimetric assay photographs for subsequent sweat chloride and pH analysis. Commercial software (Photoshop, Adobe Systems) enabled image analysis and extraction of colour values from the colorimetric assays. Error bars in each plot indicate the s.d. of data from three separate SACs or colorimetric assays. Mean values extracted

from three random points ( $n=3$ ) from the colorimetric assays yielded the chloride concentration and pH.

**Reporting Summary.** Further information on research design is available in the Nature Research Reporting Summary linked to this article.

### Data availability

The data that support the plots within this paper and other findings of this study are available from the corresponding authors upon reasonable request.

### Code availability

Custom-developed firmware for the electronic module and LabView data acquisition software for hardware characterization are available from the corresponding authors upon reasonable request.

Received: 4 January 2020; Accepted: 11 June 2020;

Published online: 13 July 2020

### References

- Ray, T. R. et al. Bio-integrated wearable systems: a comprehensive review. *Chem. Rev.* **119**, 5461–5533 (2019).
- Song, Y., Min, J. & Gao, W. Wearable and implantable electronics: moving toward precision therapy. *ACS Nano* **13**, 12280–12286 (2019).
- Bariya, M., Nyein, H. Y. Y. & Javey, A. Wearable sweat sensors. *Nat. Electron.* **1**, 160 (2018).
- Choi, J. et al. Soft, skin-integrated multifunctional microfluidic systems for accurate colorimetric analysis of sweat biomarkers and temperature. *ACS Sens.* **4**, 379–388 (2019).
- Caldara, M., Colleoni, C., Guido, E., Re, V. & Rosace, G. Optical monitoring of sweat pH by a textile fabric wearable sensor based on covalently bonded litmus-3-glycidoxypolytrimethoxysilane coating. *Sens. Actuators B* **222**, 213–220 (2016).
- Reeder, J. T. et al. Resettable skin interfaced microfluidic sweat collection devices with chemesthetic hydration feedback. *Nat. Commun.* **10**, 5513 (2019).
- Yang, Y. et al. A laser-engraved wearable sensor for sensitive detection of uric acid and tyrosine in sweat. *Nat. Biotechnol.* **38**, 217–224 (2020).
- Kim, J. et al. Simultaneous monitoring of sweat and interstitial fluid using a single wearable biosensor platform. *Adv. Sci.* **5**, 1800880 (2018).
- Khan, Y. et al. Organic multi-channel optoelectronic sensors for wearable health monitoring. *IEEE Access* **7**, 128114–128124 (2019).
- Kafi, M. A., Paul, A., Vilouras, A., Hosseini, E. S. & Dahiya, R. S. Chitosan-graphene oxide based ultra-thin and flexible sensor for diabetic wound monitoring. *IEEE Sens. J.* **13**, 6794–6801 (2019).
- Lee, K. et al. Mechano-acoustic sensing of physiological processes and body motions via a soft wireless device placed at the suprasternal notch. *Nat. Biomed. Eng.* **4**, 148–158 (2020).
- Imani, S. et al. A wearable chemical–electrophysiological hybrid biosensing system for real-time health and fitness monitoring. *Nat. Commun.* **7**, 11650 (2016).
- Yin, L. et al. Highly stable battery pack via insulated, reinforced, buckling-enabled interconnect array. *Small* **14**, 1800938 (2018).
- Liu, R. et al. Shape memory polymers for body motion energy harvesting and self-powered mechanosensing. *Adv. Mater.* **30**, 1705195 (2018).
- Mokhtari, F., Foroughi, J., Zheng, T., Cheng, Z. & Spinks, G. M. Triaxial braided piezo fiber energy harvesters for self-powered wearable technologies. *J. Mater. Chem. A* **7**, 8245–8257 (2019).
- Bandodkar, A. J. Wearable biofuel cells: past, present and future. *J. Electrochem. Soc.* **164**, H3007–H3014 (2017).
- Chen, X. et al. Stretchable and flexible buckypaper-based lactate biofuel cell for wearable electronics. *Adv. Funct. Mater.* **29**, 1905785 (2019).
- Yu, Y. et al. Biofuel-powered soft electronic skin with multiplexed and wireless sensing for human-machine interfaces. *Sci. Robot.* **5**, eaaz7946 (2020).
- Hu, X. et al. Nacre-inspired crystallization and elastic “brick-and-mortar” structure for a wearable perovskite solar module. *Energy Environ. Sci.* **12**, 979–987 (2019).
- O'Connor, T. F. et al. Wearable organic solar cells with high cyclic bending stability: materials selection criteria. *Sol. Energy Mater. Sol. Cells* **144**, 438–444 (2016).
- Li, C. et al. Flexible perovskite solar cell-driven photo-rechargeable lithium-ion capacitor for self-powered wearable strain sensors. *Nano Energy* **60**, 247–256 (2019).
- Ostfeld, A. E., Gaikwad, A. M., Khan, Y. & Arias, A. C. High-performance flexible energy storage and harvesting system for wearable electronics. *Sci. Rep.* **6**, 26122 (2016).
- Huang, X. et al. Epidermal radio frequency electronics for wireless power transfer. *Microsyst. Nanoeng.* **2**, 16052 (2016).

24. Bito, J., Hester, J. G. & Tentzeris, M. M. Ambient RF energy harvesting from a two-way talk radio for flexible wearable wireless sensor devices utilizing inkjet printing technologies. *IEEE Trans. Microw. Theory Tech.* **63**, 4533–4543 (2015).
25. Rose, D. P. et al. Adhesive RFID sensor patch for monitoring of sweat electrolytes. *IEEE Trans. Biomed.* **62**, 1457–1465 (2015).
26. Bandonkar, A. J. et al. Battery-free, skin-interfaced microfluidic/electronic systems for simultaneous electrochemical, colorimetric, and volumetric analysis of sweat. *Sci. Adv.* **5**, eaav3294 (2019).
27. Niu, S. et al. A wireless body area sensor network based on stretchable passive tags. *Nat. Electron.* **2**, 361–368 (2019).
28. Liu, W., Song, M. S., Kong, B. & Cui, Y. Flexible and stretchable energy storage: recent advances and future perspectives. *Adv. Mater.* **29**, 1603436 (2017).
29. Zhang, Y., Zhao, Y., Ren, J., Weng, W. & Peng, H. Advances in wearable fiber-shaped lithium-ion batteries. *Adv. Mater.* **28**, 4524–4531 (2016).
30. Liu, Q.-C. et al. A flexible and wearable lithium–oxygen battery with record energy density achieved by the interlaced architecture inspired by bamboo slips. *Adv. Mater.* **28**, 8413–8418 (2016).
31. Kumar, R. et al. All-printed, stretchable Zn–Ag<sub>2</sub>O rechargeable battery via hyperelastic binder for self-powering wearable electronics. *Adv. Energy Mater.* **7**, 1602096 (2017).
32. Ji, D. et al. Atomically transition metals on self-supported porous carbon flake arrays as binder-free air cathode for wearable zinc–air batteries. *Adv. Mater.* **31**, 1808267 (2019).
33. Li, H. et al. An extremely safe and wearable solid-state zinc ion battery based on a hierarchical structured polymer electrolyte. *Energy Environ. Sci.* **11**, 941–951 (2018).
34. Berchmans, S. et al. An epidermal alkaline rechargeable Ag–Zn printable tattoo battery for wearable electronics. *J. Mater. Chem. A* **2**, 15788–15795 (2014).
35. Yang, Y. et al. Waterproof, ultrahigh areal-capacitance, wearable supercapacitor fabrics. *Adv. Mater.* **29**, 1606679 (2017).
36. Rajendran, V., Mohan, A. M. V., Jayaraman, M. & Nakagawa, T. All-printed, interdigitated, freestanding serpentine interconnects based flexible solid state supercapacitor for self powered wearable electronics. *Nano Energy* **65**, 104055 (2019).
37. Lee, K. B. Urine-activated paper batteries for biosystems. *J. Microchem. Microeng.* **15**, S210–S214 (2005).
38. Koo, Y., Sankar, J. & Yun, Y. High performance magnesium anode in paper-based microfluidic battery, powering on-chip fluorescence assay. *Biomicrofluidics* **8**, 054104 (2014).
39. Ortega, L., Llorella, A., Esquivel, J. P. & Sabaté, N. Self-powered smart patch for sweat conductivity monitoring. *Microsyst. Nanoeng.* **5**, 3 (2019).
40. She, D., Tsang, M. & Allen, M. Biodegradable batteries with immobilized electrolyte for transient MEMS. *Biomed. Microdevices* **21**, 17 (2019).
41. Liu, G. et al. A wearable conductivity sensor for wireless real-time sweat monitoring. *Sens. Actuators B* **227**, 35–42 (2016).
42. Emrich, H. M. et al. Sweat composition in relation to rate of sweating in patients with cystic fibrosis of the pancreas. *Pediatr. Res.* **2**, 464–478 (1968).
43. Buono, M. J., Ball, K. D. & Kolkhorst, F. W. Sodium ion concentration vs. sweat rate relationship in humans. *J. Appl. Physiol.* **103**, 990–994 (2007).
44. Bandonkar, A. J. et al. Soft, skin-interfaced microfluidic systems with passive galvanic stopwatches for precise chronometric sampling of sweat. *Adv. Mater.* **31**, 1902109 (2019).
45. Kong, Y., Wang, C., Yang, Y., Too, C. O. & Wallace, G. G. A battery composed of a polypyrrole cathode and a magnesium alloy anode—toward a bioelectric battery. *Synth. Met.* **162**, 584–589 (2012).
46. Williams, G. & McMurray, H. N. Localized corrosion of magnesium in chloride-containing electrolyte studied by a scanning vibrating electrode technique. *J. Electrochem. Soc.* **155**, C340–C349 (2008).
47. Huang, W. et al. Nanostructural and electrochemical evolution of the solid-electrolyte interphase on CuO nanowires revealed by cryogenic-electron microscopy and impedance spectroscopy. *ACS Nano* **13**, 737–744 (2018).
48. Cong, G., Wang, W., Lai, N.-C., Liang, Z. & Lu, Y.-C. A high-rate and long-life organic–oxygen battery. *Nat. Mater.* **18**, 390 (2019).
49. Peng, G. S., Chen, K. H., Fang, H. C., Chao, H. & Chen, S. Y. EIS study on pitting corrosion of 7150 aluminum alloy in sodium chloride and hydrochloric acid solution. *Mater. Corros.* **61**, 783–789 (2010).
50. Brett, C. M. A. On the electrochemical behaviour of aluminium in acidic chloride solution. *Corros. Sci.* **33**, 203–210 (1992).
51. Choi, D.-H., Kim, J. S., Cutting, G. R. & Searson, P. C. Wearable potentiometric chloride sweat sensor: the critical role of the salt bridge. *Anal. Chem.* **88**, 12241–12247 (2016).
52. Choi, J. et al. Soft, skin-mounted microfluidic systems for measuring secretory fluidic pressures generated at the surface of the skin by eccrine sweat glands. *Lab Chip* **17**, 2572–2580 (2017).
53. Twine, N. B. et al. Open nanofluidic films with rapid transport and no analyte exchange for ultra-low sample volumes. *Lab Chip* **18**, 2816–2825 (2018).
54. Wang, R. et al. Accuracy of wrist-worn heart rate monitors. *JAMA Cardiol.* **2**, 104–106 (2017).
55. Emaminejad, S. et al. Autonomous sweat extraction and analysis applied to cystic fibrosis and glucose monitoring using a fully integrated wearable platform. *Proc. Natl Acad. Sci. USA* **114**, 4625–4630 (2017).

### Acknowledgements

This research was funded by the Air Force Research Laboratory (AFRL) Human Signatures Branch through Core funds provided to Northwestern University under contract FA8650-14-D-6516. S.W., T.H. and S.M. acknowledge support from the ‘Top Open’ programme (Tsinghua University, P. R. China), the visiting scholar programme (grant no. 201706235005, China Scholarship Council) and the Indo-US Science and Technology Forum (grant no. SERB-IUSSTF-2017/192) respectively. This work utilized the Northwestern University Micro/Nano Fabrication Facility (NUFAB), which is partially supported by the Soft and Hybrid Nanotechnology Experimental (SHyNE) resource (NSF ECCS-1542205), the Materials Research Science and Engineering Center (DMR-1720139), the State of Illinois and Northwestern University.

### Author contributions

J.A.R., A.J.B., R.G. and S.P.L. conceived the project, designed the studies and analysed and interpreted the data. A.J.B. designed and developed the batteries, microfluidics, pH sensor and chloride sensor. S.P.L. designed and developed the electronics. W.L. developed the firmware. A.J.B., I.H., S.W., T.H., S.M. and N.N. worked on testing and optimizing the batteries. S.P.L., C.-J.S. and P.G. worked on fabricating and testing of the electronics. A.J.B. and J.C. worked on fabricating the microfluidics. J.K. assisted in optical studies. W.J.J., J.T.R. and R.T. assisted in testing the devices. A.J.B., S.P.L., W.J.J., I.H., R.G. and J.A.R. composed the manuscript.

### Competing interests

J.A.R., S.P.L., W.L. and R.G. are cofounders and/or employees of Epicore Biosystems, Inc., a company that pursues commercialization of microfluidic devices for wearable applications.

### Additional information

**Supplementary information** is available for this paper at <https://doi.org/10.1038/s41928-020-0443-7>.

**Correspondence and requests for materials** should be addressed to R.G. or J.A.R.

**Reprints and permissions information** is available at [www.nature.com/reprints](http://www.nature.com/reprints).

**Publisher's note** Springer Nature remains neutral with regard to jurisdictional claims in published maps and institutional affiliations.

© The Author(s), under exclusive licence to Springer Nature Limited 2020

## Reporting Summary

Nature Research wishes to improve the reproducibility of the work that we publish. This form provides structure for consistency and transparency in reporting. For further information on Nature Research policies, see [Authors & Referees](#) and the [Editorial Policy Checklist](#).

### Statistics

For all statistical analyses, confirm that the following items are present in the figure legend, table legend, main text, or Methods section.

n/a Confirmed

- The exact sample size ( $n$ ) for each experimental group/condition, given as a discrete number and unit of measurement
- A statement on whether measurements were taken from distinct samples or whether the same sample was measured repeatedly
- The statistical test(s) used AND whether they are one- or two-sided  
*Only common tests should be described solely by name; describe more complex techniques in the Methods section.*
- A description of all covariates tested
- A description of any assumptions or corrections, such as tests of normality and adjustment for multiple comparisons
- A full description of the statistical parameters including central tendency (e.g. means) or other basic estimates (e.g. regression coefficient) AND variation (e.g. standard deviation) or associated estimates of uncertainty (e.g. confidence intervals)
- For null hypothesis testing, the test statistic (e.g.  $F$ ,  $t$ ,  $r$ ) with confidence intervals, effect sizes, degrees of freedom and  $P$  value noted  
*Give  $P$  values as exact values whenever suitable.*
- For Bayesian analysis, information on the choice of priors and Markov chain Monte Carlo settings
- For hierarchical and complex designs, identification of the appropriate level for tests and full reporting of outcomes
- Estimates of effect sizes (e.g. Cohen's  $d$ , Pearson's  $r$ ), indicating how they were calculated

*Our web collection on [statistics for biologists](#) contains articles on many of the points above.*

### Software and code

Policy information about [availability of computer code](#)

#### Data collection

On-body human data was captured on the electronic module using custom developed firmware that measures ECG, computes the heart rate and logs the heart rate to on-board EEPROM memory. To optimize the heart rate algorithm and characterize the electronic module, custom LabView software was written to capture narrow-band ECG morphology from the module's amplifier outputs using a data acquisition system (National Instruments, Austin, TX). Electrochemical characterization of the SACs was performed using an electrochemical analyser (PGSTAT128N, Metrohm, Riverview, FL). During human trials, a Samsung S7 smartphone was used to wirelessly collect the heart rate data stored in the memory of the electronic module while the phone's camera was used to capture photos of the colorimetric assays for subsequent sweat chloride and pH analysis.

#### Data analysis

Colorimetric analysis was performed using Photoshop (Adobe Systems, CA). NOVA 2.1 software provided by Metrohm was used to analyse electrochemical data acquired from SACs. Custom firmware was developed for computing heart rate from captured ECG signal, managing power consumption and storing data to memory. ST25 NFC Tap® Application software (STMicroelectronics, Switzerland) was used to wirelessly transfer heart rate data from the electronic module to an NFC-enabled smartphone (Samsung S7).

For manuscripts utilizing custom algorithms or software that are central to the research but not yet described in published literature, software must be made available to editors/reviewers. We strongly encourage code deposition in a community repository (e.g. GitHub). See the Nature Research [guidelines for submitting code & software](#) for further information.

### Data

Policy information about [availability of data](#)

All manuscripts must include a [data availability statement](#). This statement should provide the following information, where applicable:

- Accession codes, unique identifiers, or web links for publicly available datasets
- A list of figures that have associated raw data
- A description of any restrictions on data availability

The data that support the plots within this paper and other findings of this study are available from the corresponding author upon reasonable request.

## Field-specific reporting

Please select the one below that is the best fit for your research. If you are not sure, read the appropriate sections before making your selection.

Life sciences       Behavioural & social sciences       Ecological, evolutionary & environmental sciences

For a reference copy of the document with all sections, see [nature.com/documents/nr-reporting-summary-flat.pdf](https://www.nature.com/documents/nr-reporting-summary-flat.pdf)

## Life sciences study design

All studies must disclose on these points even when the disclosure is negative.

Sample size	4 consenting male subjects.
Data exclusions	No data excluded.
Replication	The devices were on the consenting human subjects to verify the reproducibility of the functioning of the devices.
Randomization	Subjects were selected from within the research group.
Blinding	Data from the human trials were performed and analysed by different authors.

## Reporting for specific materials, systems and methods

We require information from authors about some types of materials, experimental systems and methods used in many studies. Here, indicate whether each material, system or method listed is relevant to your study. If you are not sure if a list item applies to your research, read the appropriate section before selecting a response.

### Materials & experimental systems

### Methods

n/a	Involvement in the study
<input checked="" type="checkbox"/>	<input type="checkbox"/> Antibodies
<input checked="" type="checkbox"/>	<input type="checkbox"/> Eukaryotic cell lines
<input checked="" type="checkbox"/>	<input type="checkbox"/> Palaeontology
<input checked="" type="checkbox"/>	<input type="checkbox"/> Animals and other organisms
<input type="checkbox"/>	<input checked="" type="checkbox"/> Human research participants
<input checked="" type="checkbox"/>	<input type="checkbox"/> Clinical data

n/a	Involvement in the study
<input checked="" type="checkbox"/>	<input type="checkbox"/> ChIP-seq
<input checked="" type="checkbox"/>	<input type="checkbox"/> Flow cytometry
<input checked="" type="checkbox"/>	<input type="checkbox"/> MRI-based neuroimaging

## Human research participants

Policy information about [studies involving human research participants](#)

Population characteristics	Healthy male subjects in the age range of 20-40 years.
Recruitment	Consenting male subjects were recruited from within the research group.
Ethics oversight	Institutional Review Board at Northwestern University.

Note that full information on the approval of the study protocol must also be provided in the manuscript.